Fuel 413 (2026) 138309

Contents lists available at ScienceDirect

Fuel

journal homepage: www.elsevier.com/locate/fuel

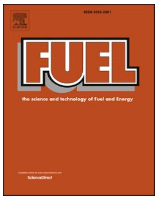

Full Length Article

Electrosynthesis of nickel nanostructure via electrochemical dealloying technique and its applicability toward HER and OER

Narjes Ramezanian, Mostafa Mirjalili *, Ghasem Barati Darband

Department of Materials Science and Engineering, Faculty of Engineering, Ferdowsi University of Mashhad, Mashhad 91779-48974, Iran

ARTICLE INFO

Keywords:
Ni-Cu electrocatalyst
Electrochemical dealloying
Water splitting
Hydrogen evolution reaction
Oxygen evolution reaction

ABSTRACT

Developing cost-effective electrocatalysts for efficient water splitting is crucial for sustainable hydrogen production. This research reports the synthesis of nanostructured Ni–Cu electrodes via electrochemical deposition followed by selective dealloying. The dealloying process produced a unique coral-like morphology, greatly enhancing the electrochemically active surface area. Interestingly, the optimal deposition current density differed for the two half-reactions: the sample deposited at 50 mA cm^{-2} showed superior HER activity (η_{10}= 57 mV, Tafel slope = 65 $mV.dec^{-1}$), while the 100 mA cm^{-2} sample demonstrated the best OER performance (η_{10} = 259 mV, Tafel slope = 55.5 $mV.dec^{-1}$). A two-electrode configuration using the optimized samples required only 1.55 V to deliver 10 mA cm^{-2}, outperforming many reported Ni-based dealloyed systems. These results highlight that tuning the electrodeposition current density provides a simple yet powerful strategy to tailor bifunctional Ni–Cu electrocatalysts for overall water splitting. Beyond performance optimization, this work provides mechanistic clarification of the unexpected selective dissolution of Cu during dealloying. Although Cu is more noble than Ni, this work shows that the formation of a protective passivation layer of Ni suppresses Ni dissolution, thereby promoting preferential Cu removal and leaving behind a Ni-rich porous framework.

1. Introduction

Energy and the environment are two key components of modern society, essential for the social sustainability and economic development of the world [1,2]. Recently, with population growth and the advancement of human societies, the demand for fossil fuels, like coal, petroleum oil, and natural gas – resources that are neither environmentally friendly nor renewable – has increased [3,4]. However, the consumption of fossil fuels significantly contributes to greenhouse gas emissions and causes severe environmental pollution. Furthermore, fossil fuel resources are rapidly depleting [5]. To address these challenges, global efforts have been directed toward discovering clean and renewable alternatives to fossil fuels. Different renewable and clean energy sources have been proposed. However, these energy sources are limited by intermittent accessibility due to regional or seasonal factors [6]. Therefore, an efficient renewable energy source and storage system is essential for large-scale utilization [1]. Hydrogen (H_2) is widely recognized as the most promising and environmentally friendly energy carrier, offering a viable alternative to fossil fuels [7,8]. The advantages of hydrogen include zero environmental pollution, high energy density, and various and effective synthesis methods, make it superior to other renewable energy sources [9]. Hydrogen can be produced using various methods, some of which release hazardous gases, such as CO_2 and CO, into the environment. An effective method for hydrogen production is electrochemical water splitting [10,11]. This process does not release greenhouse gases into the atmosphere and utilizes water, which is a low-cost, renewable, and abundant resource [12–15].

The overall water splitting includes two half-cell reactions: hydrogen evolution reaction (HER) on the cathode, which produces H_2, and oxygen evolution reaction (OER) on the anode, which produces O_2. The minimum theoretical potential required to initiate electrochemical water splitting is 1.23 V, and an energy input of $\Delta G^\circ = 237.1$ kJ mol^{-1}. However, a significant challenge limiting the efficiency of water splitting is the sluggish kinetics of both HER and OER. These reactions require high overpotentials due to various resistances, such as charge transfer resistance, the resistance caused by gas bubbles generated on the surface of catalyst, and the resistance of the electrolyte. Consequently, the actual potential required to initiate water splitting is much higher than 1.23 V [16–19]. Synthesizing effective electrocatalysts is a critical strategy for reducing the high overpotentials at the surfaces of

---

* Corresponding author.
E-mail address: mirjalili@um.ac.ir (M. Mirjalili).

https://doi.org/10.1016/j.fuel.2026.138309
Received 28 September 2025; Received in revised form 17 December 2025; Accepted 6 January 2026

the anode and cathode. It is reported that the best electrocatalysts for HER and OER are noble metal-based such as platinum, and IrO_2 or RuO_2, respectively. [20]. However, limited availability of these materials and the high cost constrain their widespread application [21–23]. This has driven researchers to design and develop cost-effective and non-noble metal-based electrocatalysts.

An effective electrocatalyst for water splitting must have different characterization including: high intrinsic electrocatalytic activity, good conductivity, electrochemical stability, excellent corrosion resistance, and a large active surface area [24–27]. Intrinsic electrocatalytic activity can be enhanced by utilizing compounds with inherently high electrocatalytic activity. Electrocatalysts based on transition metals, such as Pt, Co, Ni, Mo, Fe, and Cu, demonstrate excellent intrinsic electrocatalytic activity [28]. Among these metals, Ni and its alloys are more cost-effective than noble metals like platinum and exhibit suitable electrocatalytic performance as well as chemical stability in alkaline solutions. Extensive research has been conducted on Ni-based electrocatalysts, employing various synthesis methods such as electrodeposition, hydrothermal processes, and sol–gel techniques [29–31]. However, some of these methods require specialized equipment, highlighting the need to explore simpler and more cost-effective approaches for producing electrocatalysts at an industrial scale.

On the other hand, nano-structured electrocatalysts have gained significant attention for their ability to enhance the active surface area. Studies indicate that nano-structured electrodes effectively improve electron and mass transfer, and significantly reduce the overpotential required for electrochemical water splitting [32,33]. A promising approach for producing nanostructured electrocatalysts is electrochemical dealloying, a robust technique that exploits the variance in standard electrochemical potentials between alloy components in a solution to enable selective dissolution [34–36]. During this process, an anodic potential is applied to the alloy, causing the component with a more negative electrode potential to lose electrons and dissolve in the solution, while the component with a more positive electrode potential is retained. Essentially, the less noble element is removed selectively, while the noble element transforms into a porous structure [37]. The morphology of the resulting materials can be adjusted by controlling the applied current or voltage, offering versatility in the fabrication process. Additionally, this method is advantageous due to its low experimental requirements, simplicity, and scalability [38,39].

Previous researches on the dealloying of Ni and Cu has demonstrated promising results for HER. Specifically, dealloyed Ni-Cu electrodes exhibit favorable electrocatalytic properties for HER due to the desirable intrinsic properties of Ni and the high electrochemical active surface area created by the selective dissolution of Cu during dealloying [38,40,41]. Limited studies have been conducted on dealloyed Ni-Cu electrodes for the HER, especially for OER and the overall electrochemical water splitting process. For efficient water splitting, electrocatalysts must exhibit favorable electrocatalytic activity for both HER and OER to minimize overall overpotential. The OER is kinetically more challenging than the HER. Therefore, developing electrocatalysts that efficiently facilitate both HER and OER in the same environment is crucial. Such advancements would simplify electrocatalyst production and significantly reduce costs [32,42–44].

Interestingly, there is no definitive mechanism for the dealloying process of Ni and Cu. Based on standard reduction potentials, it would be expected that Ni dissolves during dealloying because Ni has a more negative reduction potential and is more electrochemically active. However, practical observations showed that Cu is preferentially dissolved from the structure [40,45,46]. This phenomenon warrants further investigation to elucidate the underlying mechanisms.

The aim of this research is to fabricate a nano-structured Ni-Cu electrocatalyst via electrochemical dealloying on a nickel foam (NF) conductive substrate for use in electrochemical water splitting. The dealloying conditions and the effect of current density of deposition on the electrocatalytic activity were systematically investigated. Additionally, the mechanism of the dealloying process for the Ni-Cu electrode was studied. Finally, electrocatalytic activity of the dealloyed Ni-Cu electrodes was investigated for HER, OER and the overall water splitting reaction.

2. Experimental

2.1. Electrodeposition process

To prepare the electrodeposition bath, 0.5 M nickel (II) sulfate hexahydrate ($NiSO_4{\cdot}6H_2O$) and 0.075 M copper (II) sulfate pentahydrate ($CuSO_4{\cdot}5H_2O$) were used as sources of Ni and Cu ions, respectively. Additionally, 0.5 M boric acid (H_3BO_3) was dissolved as a pH stabilizer in deionized water. All chemicals were laboratory-grade without further purification. The pH of electrodeposition bath was 4 and electrodeposition temperature was 30^{o}C. The electrodeposition was conducted in a two-electrode system by using a rectifier. NF with dimensions $0.3 \times 10 \times 10$ mm was used as substrate. Prior to electrodeposition, the NF was pretreated by ultrasonicating in ethanol for 10 min, followed by immersion in 5 M hydrochloric acid (HCl) for 12 min to remove oxide layer of the surface. Finally, the NF was thoroughly rinsed with distilled water. Two parallel Ni plates were used as the anodes, and the prepared NF was located between them as the cathode. Galvanostatic electrodeposition of Ni-Cu on the NF was performed for 600 s at four different cathodic current densities of 25, 50, 100, and 150 $mA.cm^{-2}$. After deposition, electrochemical dealloying was conducted at a constant potential of + 1 V for 400 s in the same solution. Subsequently, the electrocatalysts were rinsed with deionized water and air-dried. Fig. 1 illustrates the schematic of synthesis steps for the dealloyed Ni-Cu electrocatalysts. The electrodeposited and dealloyed samples were named as I25, I50, I100, and I150, respectively. Also, I50-BD and I100-BD refer to the samples before dealloying.

2.2. Morphological and electrochemical characterizations

Field-emission scanning electron microscopy (FESEM, MIRA3 TESCAN) was utilized to analyze the microstructure and morphology of the samples. Energy-dispersive X-ray spectroscopy (EDS) and elemental mapping were employed to detect chemical composition and elemental distribution of electrodes. X-ray diffraction (XRD) analysis was used to analyze the phase structure and specimens' surface chemistry of the samples with XMD–300 X-ray diffractometer with a scan angle 2θ from 10 to 90∘. Raman spectroscopy was performed using a UniDRON spectrometer with a scanning range of $300 \sim 1500$ cm^{-1} to examine the phase and chemical bonds under an excitation wavelength of 532 nm.

Electrochemical analyses were conducted in a three-electrode system using 1 M KOH as the electrolyte and Zive Sp1 potentiostat. The counter electrode was platinum plate, the reference electrode was Ag/AgCl, and the synthesized electrocatalysts were used as the working electrodes. Linear sweep voltammetry (LSV) was carried out with a scan rate of 5 $mV.s^{-1}$. The cyclic voltammetry (CV) examinations were accomplished to evaluate electrochemical active surface area (ECSA) within a range of ± 40 mV around the open-circuit potential (OCP) at scan rates from 5 to 50 $mV.s^{-1}$. Moreover, the electrochemical impedance spectroscopy (EIS) was conducted over a frequency range of 100 kHz to 100 mHz at cathodic potentials of −170, −270, and −370 mV vs. RHE for HER, and at 1625 mV vs. RHE for OER. The chronopotentiometry was conducted to assess the stability of the electrocatalysts under a constant current density of −100 and 100 $mA.cm^{-2}$ for 50 h for HER and OER, respectively. Finally, electrochemical water splitting examination was carried out using a two-electrode system. In this setup, optimal samples for OER and HER were employed as the anode and cathode, respectively. Then a chronopotentiometry was carried out at a constant current density of 10 $mA.cm^{-2}$ for 100 h to assess the stability of the optimal samples for overall water splitting. All reported potentials in electrochemical results

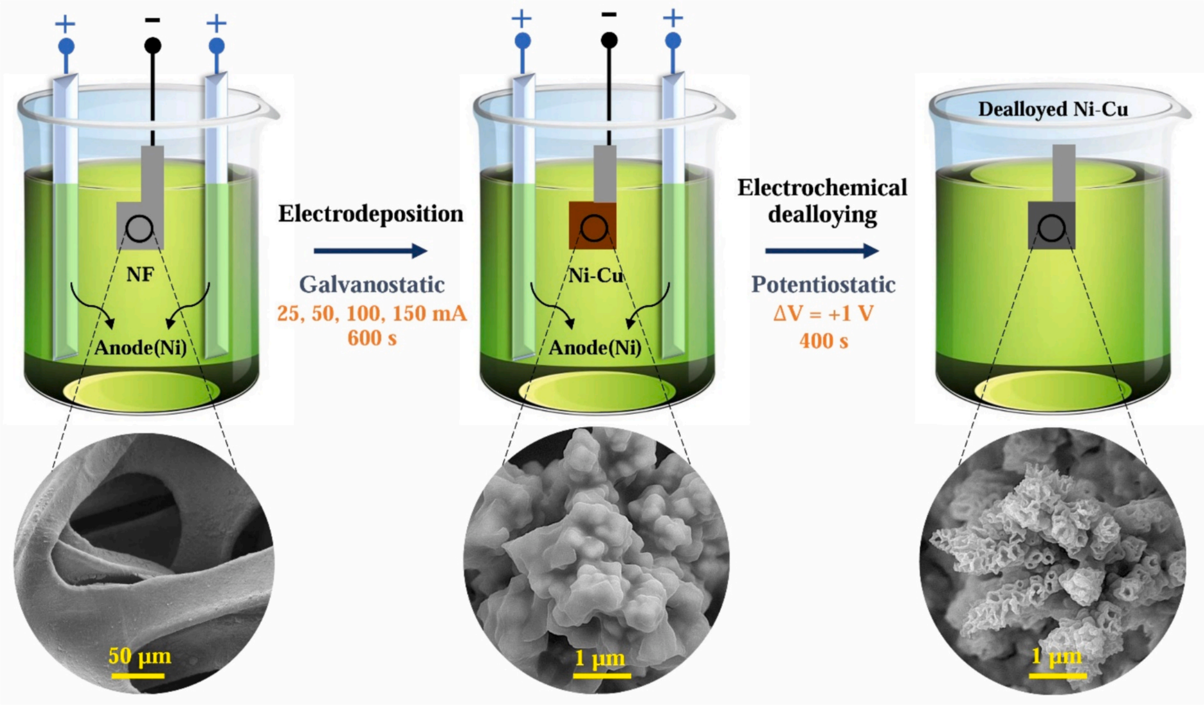

Fig. 1. A schematic of the synthesis steps of dealloyed Ni-Cu electrocatalysts.

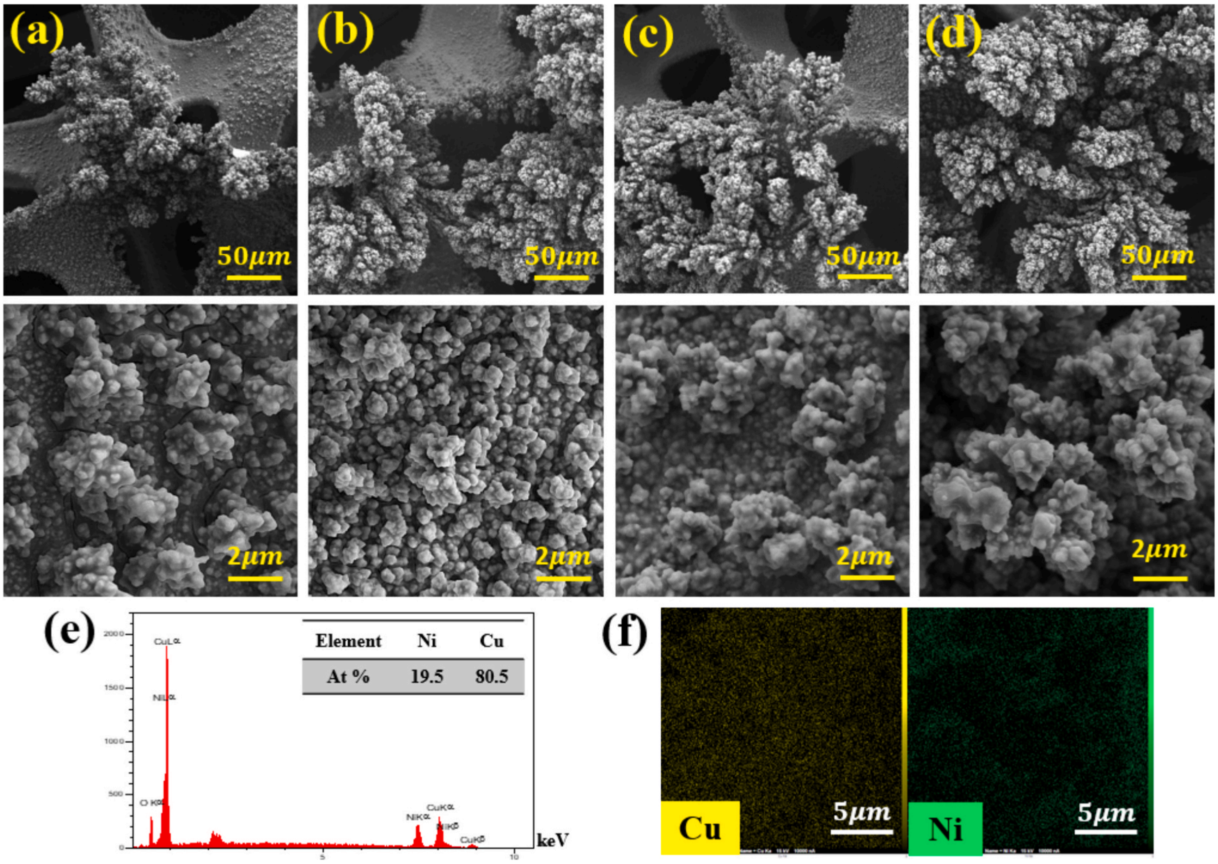

Fig. 2. FESEM images of pre-dealloyed Ni electrodes synthesized at electrodeposition current densities of (a) 25, (b) 50, (c) 100, (d) 150 mA.cm^{-2}, (e) EDS analysis of sample I50, and (f) elemental mapping images of Cu and Ni before dealloying.

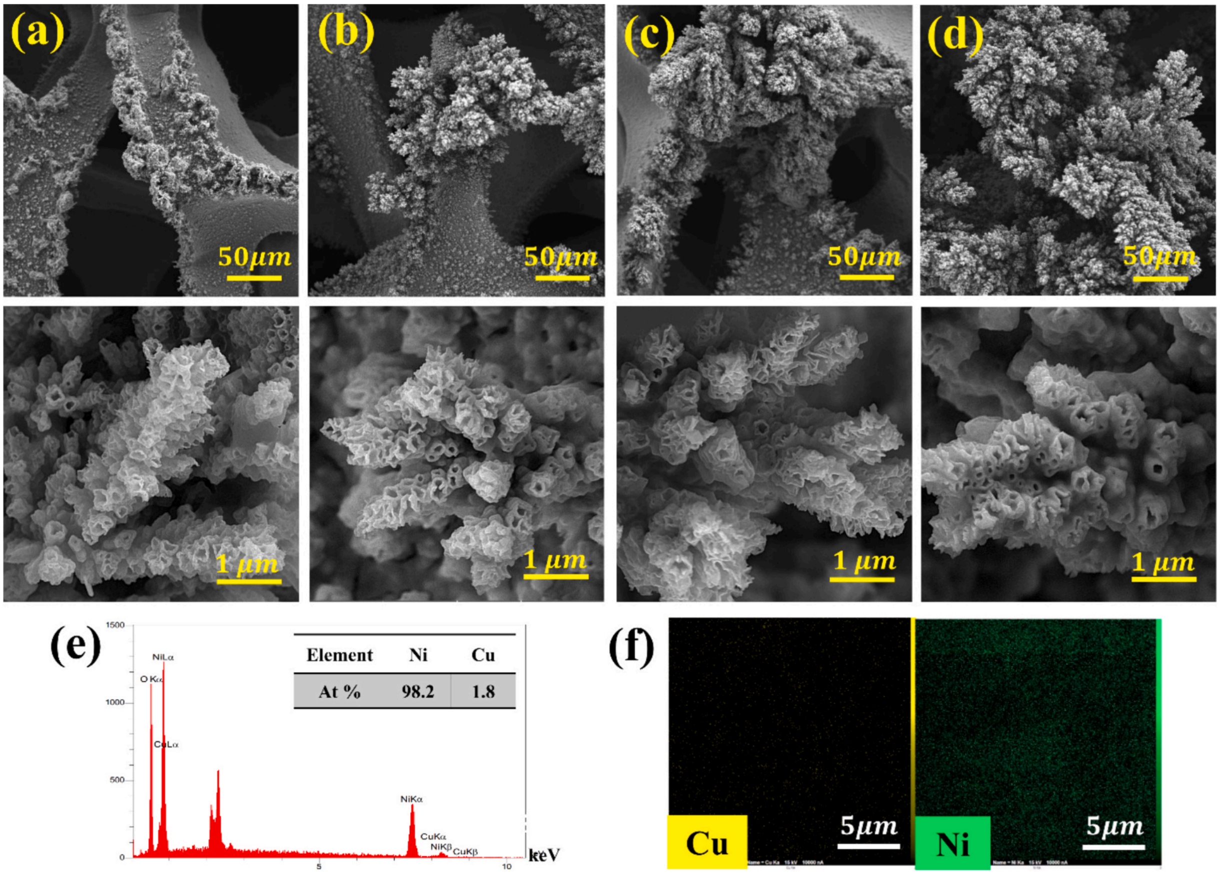

Fig. 3. FESEM images of dealloyed Ni-Cu electrodes synthesized at deposition current densities of (a) 25, (b) 50, (c) 100, (d) 150 mA.cm^{-2}, (e) EDS analysis of sample I50, and (f) elemental mapping images of Cu and Ni after dealloying.

were converted to the reversible hydrogen electrode (RHE) using Eq. (1):

$$E(\text{vs. RHE}) = E(\text{vs. Ag/AgCl}) + E^{0}_{\text{Ag/AgCl}}(197\,\text{mV}) + 59.2\,\text{pH} \quad (1)$$

3. Results and discussion

3.1. Morphology and composition

The surface microstructure of the samples was characterized by FESEM. Initially, the microstructure of the Ni-Cu layer on NF was examined. FESEM images of the Ni-Cu layer deposited at different deposition current densities on NF are represented in Fig. 2a–d at two different magnifications. According to these images, the Ni-Cu layer on NF exhibited a non-uniform structure. At the edges of the NF, the growth and density of the Ni-Cu layer were higher than other areas. This non-uniformity can be ascribed to higher distribution of electrons on the edges rather than other parts of the NF. Specifically, the accumulation of electric charge at the edges of the NF led to greater density and growth of the electrocatalyst in these regions [47]. Furthermore, as the cathodic deposition current density increased from 25 to 150 mA.cm^{-2}, the amount of deposited Ni-Cu on the NF also increased. A higher deposition current density delivers more electrons to the cathode surface (NF), resulting in the deposition of more Cu and Ni cations. Consequently, a thicker coating formed on the cathode. As depicted in Fig. 2a, the amount of Ni-Cu coating on the NF was insufficient at lower current densities, whereas Fig. 2d demonstrated a substantially thicker coating and greater coverage at higher current densities.

The EDS analysis results and the chemical composition of the Ni-Cu layer are shown in Fig. 2e. The results indicated the atomic percentage of Cu was significantly higher than Ni. The standard reversible potentials for Ni and Cu are −257 mV and 342 mV vs. SHE, respectively. Thus, Cu is much more noble than Ni. A more positive standard potential indicates a greater tendency for reduction. Therefore, despite the high concentration of Ni in the electrolyte, Cu is more likely to be reduced and deposited on the surface. Fig. 2f represents the elemental mapping analysis of the I50 sample before dealloying. The results revealed a homogeneous and uniform distribution of Ni and Cu in the electrode structure.

The morphology of the dealloyed Ni-Cu electrodes was also investigated. FESEM images of the dealloyed Ni-Cu electrodes at four different deposition current densities are shown in Fig. 3a–d at two magnifications. The most significant change observed in the morphology after dealloying was the fabrication of a coral-like structure, which significantly enhances the active surface area. This structure formed due to the selective dissolution of Cu from the Ni-Cu layer, creating a nanoporous structure. The EDS analysis results and the chemical composition of the dealloyed Ni-Cu electrode are represented in Fig. 3e. The result clearly showed a substantial decrease in the atomic percentage of Cu after dealloying. Before dealloying, the atomic percentages of Ni and Cu were 19.5 % and 80.5 %, respectively, whereas after dealloying, these values reached to 98.2 % and 1.8 %. This reduction was due to the anodic and selective dissolution of Cu from the electrode structure during electrochemical dealloying. Fig. 3f displays the elemental map analysis of the I50 sample after dealloying, confirming a homogeneous and uniform distribution of Ni in the electrode structure. Although the initial Ni–Cu alloy appeared uniform in EDS mapping, microscopic heterogeneities existed in the form of Ni-rich and Cu-rich clusters, consistent with the

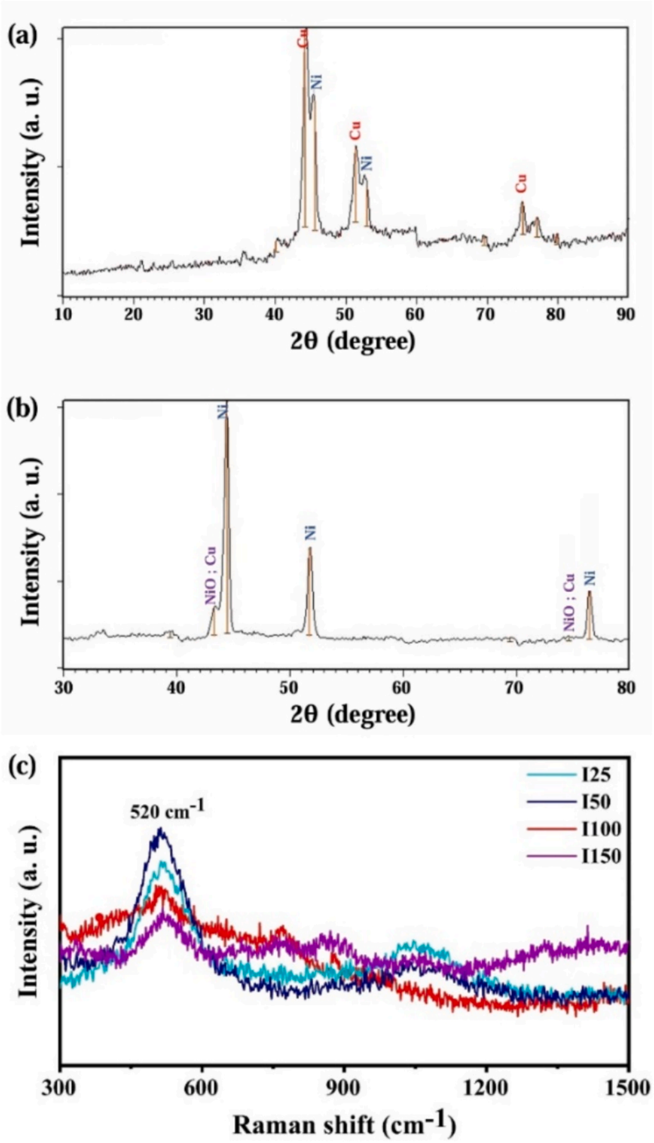

Fig. 4. XRD patterns of (a) pre-dealloyed, and (b) dealloyed sample I50, and (c) Raman spectra of samples I25, I50, I100,a and I150.

Ni–Cu phase diagram under low-temperature electrodeposition conditions. During dealloying, preferential dissolution of Cu-rich regions created localized vacancies that coalesced into micropores, resulting in the coral-like nanostructure observed.

Fig. 4a and b show the XRD patterns of the Ni–Cu electrode before and after dealloying. Before dealloying, distinct peaks at $2\theta \approx 43^\circ$, 50–52°, and 74–76° correspond to the (1 1 1), (2 0 0), and (2 2 0) planes of fcc Cu and Ni. The strong Cu signals indicate a Cu-rich alloy layer, consistent with EDS results, and the overlap of Cu/Ni peaks reflects their similar fcc structures. After dealloying, Cu-related peaks are almost completely suppressed, confirming selective Cu dissolution, while Ni peaks become sharper and more intense due to the formation of a Ni-rich framework. Weak features around $2\theta \approx 39^\circ$, 43, and 74° are attributed to a thin NiO/Ni(OH)$_2$ surface layer formed under anodic conditions which are indexed to the (1 1 1), (2 0 0) and (3 1 1). No new phases appear after dealloying, indicating retention of the metallic fcc Ni structure and the absence of Cu oxides or Ni–Cu intermetallics. These results confirm that dealloying proceeds through preferential Cu removal, leaving a porous Ni-rich skeleton—consistent with FESEM morphology and increased ECSA. The XRD evolution supports the proposed mechanism in which Cu dissolves while Ni is protected by rapid NiO passivation [48]. Fig. 4c shows the Raman spectrum of the samples I25, I50, I100, and I150. All samples show a dominant peak centered at 520 cm^{-1}, which is typically attributed to the Ni-O vibrational modes, corresponding to NiO. The presence of this peak is consistent with partial surface oxidation of Ni, which is common for dealloyed Ni-rich materials. Sample I50 shows the highest peak intensity and the sharpest spectral feature, indicating a higher amount of surface Ni-O species. This increased intensity is consistent with the enhanced porosity and Ni-rich hierarchical morphology observed in FESEM, which provides more exposed active sites for surface oxidation and Raman scattering. Sample I25 exhibits a relatively weak Raman signal, corresponding to its lower surface coverage and less-developed porous morphology. Samples I100 and I150 show broader peaks with lower intensity compared to I50, suggesting the formation of thicker or more compact surface layers, in agreement with the FESEM observations that higher deposition currents lead to denser coatings with reduced active surface area. In addition, all samples show a broad background extending from ~ 700 to 1100 cm^{-1}, which is typical of defect-rich or amorphous NiO [48,49].

Dealloying is a method in which the more active components are selectively dissolved from an alloy. Consequently, the dealloyed structure usually consists of the remaining noble elements. However, in this study, the noble element Cu dissolved, while the more active element Ni remained in the structure. To determine the cause of this behavior, a linear sweep voltammetry examination was conducted in the anodic region. Anodic polarization curves were plotted for Ni, Cu, and the Ni-Cu alloy in the same solution over a potential range from 0 to + 1500 mV vs. SCE. The results are shown in Fig. 5. According to the results, Cu exhibited a higher anodic current density, whereas Ni showed a very low anodic current density. This low current density is because of formation of a passive oxide layer on the surface of Ni. The formed NiO layer on the surface of Ni acted as a protective barrier, preventing its dissolution during anodic dissolution and dealloying [45]. Thus, although Cu had a more positive standard electrochemical potential and was more noble, it exhibited higher dissolution rate compared to Ni. Therefore, Cu dissolved from the structure during dealloying and a nanoporous Ni-rich structure was remained.

The selective dissolution of Cu from Cu–Ni alloys can be rationalized by a coupled dealloying–passivation process. In the early stage, copper is the preferentially anodic element and dissolves from low-coordination surface sites and grain boundaries, consistent with a microscopic galvanic mechanism of dealloying [50,51]. The anodic reactions proceed as:

$$Cu \rightarrow Cu^{+} + e^{-} \qquad (2)$$

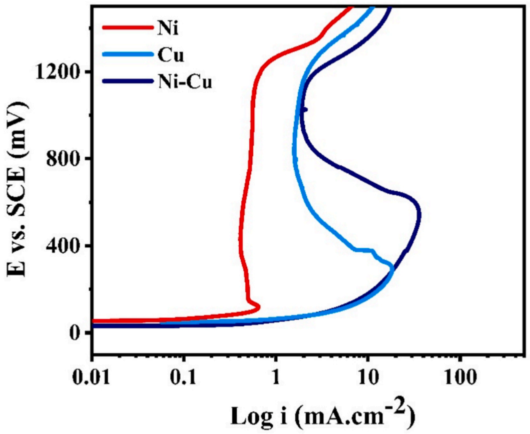

Fig. 5. Anodic polarization curves for Ni, Cu, and Ni-Cu.

$$Cu^{+} \rightarrow Cu^{2+} + e^{-} \quad (3)$$

The corresponding cathodic reaction is oxygen reduction in acidic environment:

$$O_2 + 4H^{+} + 4e^{-} \rightarrow 2H_2O \quad (4)$$

This leads to an initial burst of Cu dissolution, as confirmed by rapid increases in dissolved Cu concentration [52]. Simultaneously, Ni undergoes partial oxidation:

$$Ni \rightarrow Ni^{2+} + 2e^{-} \quad (5)$$

Although Ni^{2+} is more soluble in acidic solution than under alkaline conditions, a fraction of the Ni ions hydrolyze near the metal/solution interface and contribute to thin $Ni(OH)_2$/NiO-rich films [5,6]. Moreover, as Cu is selectively leached, the alloy surface becomes enriched in Ni, which favors the stabilization of this passive layer. The Ni-enriched film impedes further Cu dissolution by decreasing electronic and ionic transport across the interface. Thus, the overall mechanism consists of: (i) preferential anodic dissolution of Cu with stabilization of soluble Cu complexes in acidic media, (ii) progressive Ni oxidation and surface enrichment, and (iii) development of a Ni-rich passive film that suppresses subsequent dissolution.

3.2. *Hydrogen evolution reaction investigation*

The results of the LSV examination for different dealloyed samples are shown in Fig. 6a. Tafel curves and the demanded overpotential to achieve the current densities of −10, −20, and −100 $mA.cm^{-2}$ for each sample are represented in Fig. 6b and 6c, respectively. Based on the results, the best electrocatalytic properties were observed in the sample I50, with η_{10}, η_{20}, and η_{100} values of 57, 88, and 169 mV, respectively. Initially, for sample I25, the low amount of current density resulted in limited coverage on the NF surface (Fig. 3a) and consequently a limited active surface area, that leads to a weak electrocatalytic properties. As the current density of electrodeposition increased, the mass of deposited layer on the NF surface increased and more coating coverage was observed. However, the deposited layer exhibited a more convoluted and thicker morphology which may lead to lower active surface area.

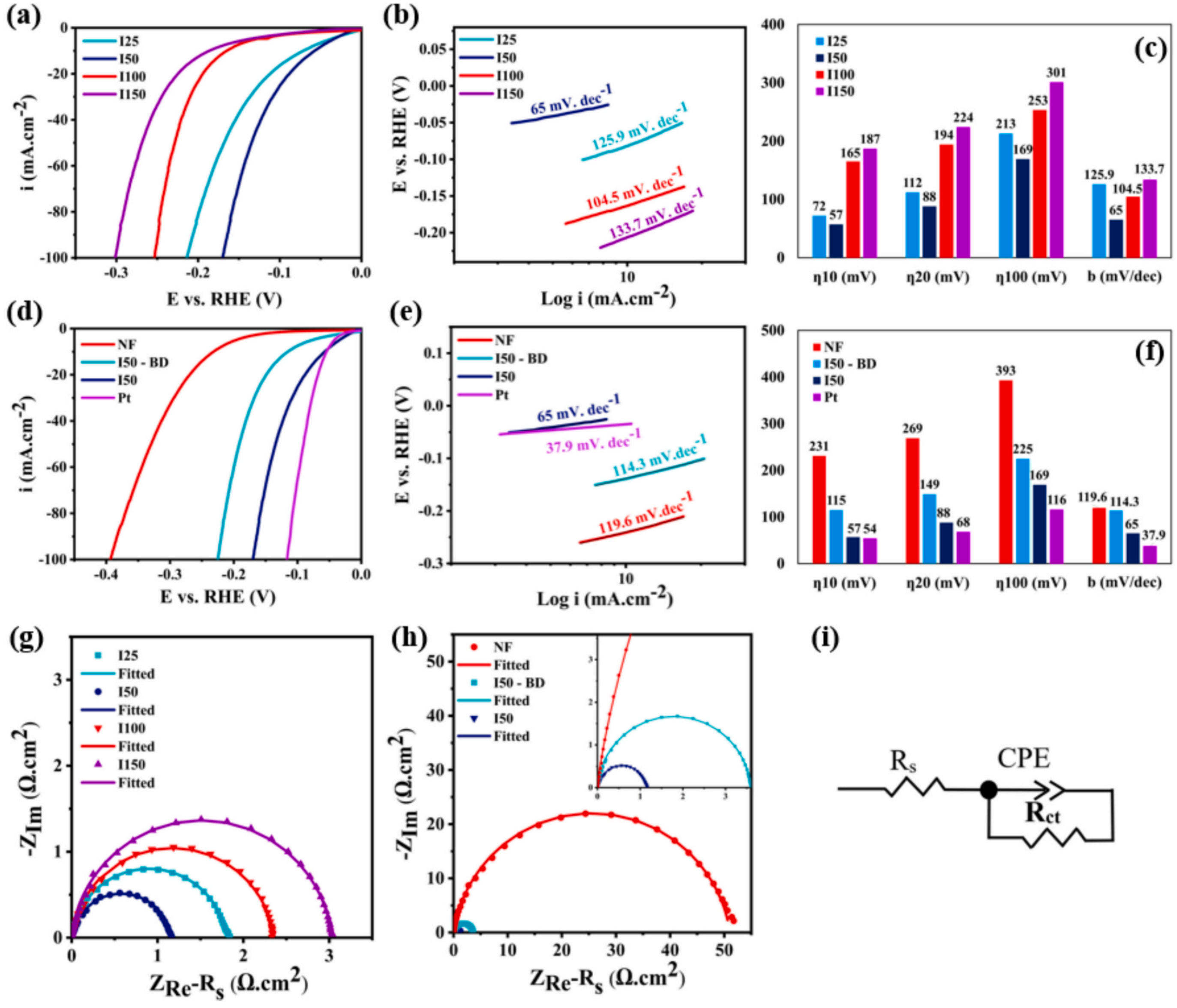

Fig. 6. (a) iR corrected LSV curves, (b) Tafel slopes, and (c) required overpotentials of dealloyed samples. (d) iR corrected LSV curves, (e) Tafel slopes and (f) required overpotentials of samples NF, I50-BD, I50, and Pt in 1.0 M KOH solution, (g) Nyquist curves of the dealloyed samples and (h) different samples at applied potential of −170 mV vs. RHE, and (i) The equivalent circuit.

Therefore, an optimum current density of electrodeposition is needed to reach the highest electrochemical active surface area. In sample I50, an optimal condition for both the surface coverage and thickness was achieved, causing the highest electrocatalytic properties.

To investigate HER rate, the Tafel slope was measured. According to Eq. (6), the Tafel slope suggested the relationship between the overpotential and the logarithm of current density [53–55]:

$$\eta = b\log i + a \tag{6}$$

where *b*, *i*, and *a* are the Tafel slope, current density, and charge transfer coefficient. A lower Tafel slope shows a superior electrocatalytic behavior. Tafel slope is also regarded as an inherent characteristic for studying the mechanism of the HER and the rate-determining step (RDS). The HER is a multi-step process that involves the transfer of two electrons on the surface of cathode. In the electrochemical water splitting process, in both alkaline and acidic environments, this reaction is divided into three stages: the Volmer, Heyrovsky, and Tafel reactions, as reported below [56]:

$$H_2O + e^- \rightarrow H_{ads} + OH^- (\mathit{Electrochemicaladsorptionofhydrogen}, \mathit{Volmerreaction}) \tag{7}$$

$$H_{ads} + H_2O + e^- \rightarrow H_2 + OH^- (\mathit{Electrochemicaldesorptionofhydrogen}, \mathit{Heyrovskyreaction}) \tag{8}$$

$$H_{ads} + H_{ads} \rightarrow H_2 (\mathit{Chemicaldesorptionofhydrogen}, \mathit{Tafelreaction}) \tag{9}$$

These reactions occur on cathode surface. Tafel slopes have been approximately reported 29, 39, and 118 $mV.dec^{-1}$ when the RDS is Tafel, Heyrovsky, and Volmer stage, respectively [33,55].

As shown in Fig. 6b, Tafel slope of sample I50 is 65 $mV.dec^{-1}$ which is the lowest Tafel slope among all samples. The lower Tafel slope in this sample suggested higher hydrogen production rate compared to the other samples. Furthermore, since Tafel slope of sample I50 is between those of Volmer and Heyrovsky stages (i.e., 118 and 39 $mV.dec^{-1}$, respectively), the overall reaction is under a mix-controlled condition. In contrast, the Volmer step was the RDS for samples I25, I100 and I150. Table S1 represents a comparison of the electrocatalytic properties of the I50 sample with the results from literature which synthesized Ni-based electrocatalysts.

To examine the effect of dealloying on the electrocatalytic properties of Ni-Cu electrode, the LSV results and Tafel slopes of the best sample (I50) before and after dealloying, along with results for NF and platinum, were evaluated. The LSV results are represented in Fig. 6d, and the Tafel slopes and the required overpotential values for each sample are shown in Fig. 6e and 6f, respectively. Based on the LSV results, it was observed that by depositing a Ni-Cu coating on NF, the electrocatalytic activity improved, and required overpotential to achieve the current density of −10 $mA.cm^{-2}$ decreased from 231 to 115 mV. After dealloying, it was observed that the electrocatalytic activity significantly improved, and the required overpotentials were 57, 88, and 169 mV for reaching current densities of −10, −20, and −100 $mA.cm^{-2}$, respectively. These values were very close to those obtained for platinum plate, which were 54, 68, and 116 mV, respectively. These results indicated that formation of a nanostructured microporous morphology after dealloying increased the electrochemical catalytic activity. Thus, formed hydrogen bubbles detach easily from the surface resulting in a significant reduction in bubble resistance and the required overpotential. Moreover, formation of a Ni-rich layer containing low amounts of Cu is believed to have a proper intrinsic catalytic activity [33].

EIS is an important technique to evaluate the interface properties of catalysts and the HER kinetics on surfaces. Fig. 6g represents obtained Nyquist curves from the EIS examination of different samples at potential of −170 mV vs. RHE. Randles circuit (Fig. 6i) was used to fit the Nyquist curves, which consisted of charge transfer resistance (R_{ct}), electrolyte resistance (R_s), and a constant-phase element (CPE), defined by following equation [57]:

$$Z_{CPE} = \frac{1}{Q\,(i\omega)^n} \tag{10}$$

where n and Q are the CPE exponent and constant, respectively, and ω is the angular frequency ($rad.s^{-1}$). The extracted electrochemical parameters from EIS results are represented in Table S2. According to this table, the values of R_{ct} for the dealloyed samples I25, I50, I100, and I150 were 1.808, 1.164, 2.36, and 3.038 $\Omega.cm^2$, respectively. The lower charge transfer resistance of I50 indicated a higher hydrogen production rate compared to the other samples, which was confirmed by the LSV results. Nyquist curves of the different samples at three different potentials (−170, −270, and −370 mV vs. RHE) can be seen in Fig. S1. As shown in this figure, as the potential became more negative, the diameter of the Nyquist curves and R_{ct} decreased. Therefore, by reducing R_{ct}, the hydrogen production rate increases at higher overpotentials.

To investigate the effect of dealloying on R_{ct}, the Nyquist curves for NF and sample I50 before and after dealloying are plotted at a potential of −170 mV vs. RHE (Fig. 6h), and the electrochemical parameters are represented in Table S2. The values of R_{ct} for NF, I50-BD, and I50 were 51.1, 3.59, and 1.164 $\Omega.cm^2$, respectively. As can be seen, NF had the highest R_{ct}, indicating poor electrocatalytic activity. After the electrodeposition of Ni-Cu, R_{ct} has decreased significantly. Moreover, a further decrease was observed in R_{ct} due to the dealloying, demonstrating an improvement in electrocatalytic activity.

The electrochemical active surface area (ECSA) of the samples was estimated using C_{dl} assessed via cyclic voltammetry (CV) examinations at diverse sweep rates in the non-Faradaic region around the open circuit potential (OCP) [58]. The potential range was ± 40 mV around the OCP (Fig. 7a–d). According to Eq. (11), C_{dl} was estimated by calculating and plotting the average absolute value of cathodic and anodic current density at the maximum and minimum potential (i_{avg}) versus the sweep rate (dV/dt) (Fig. 7e) [55].

$$i_{avg} = C_{dl}\frac{dV}{dt} \tag{11}$$

The ECSA of each sample was then evaluated by dividing the value of C_{dl} by 20 μF (the nominal capacitance of a uniform metallic surface). Fig. 7f shows the ECSA values for each sample. The results indicated that the highest C_{dl} and the largest ECSA were observed for sample I50. At lower current density (i.e., sample I25), the surface coverage is not completed (according to FESEM image in Fig. 3a) and thus the ECSA is low. By increasing the current density to 50 $mA.cm^{-2}$, ECSA has increased to a maximum value. However, further increase in the deposition current density resulted in a decrement in the ECSA of the samples. As indicated in FESEM images (Fig. 3c and d), higher current density of electrodeposition causes a more convoluted and thicker morphology which may lead to lower active surface area due to pore elimination. In sample I50, an optimal condition for surface coverage and maximum porosity was achieved, resulting in the largest ECSA and the highest electrocatalytic activity.

To further investigate the effect of dealloying on the ECSA of electrocatalysts, CV examinations were conducted on the NF and the sample I50 before and after dealloying (Fig. S2). Based on results, the C_{dl} values for NF, I50-BD, and I50 were 0.398, 5.01, and 11.53 $mF.cm^{-2}$, respectively. As shown, applying a Ni-Cu coating to the NF increased the ECSA from 19.9 to 250.5 $cm^2.cm^{-2}$. After dealloying, the ECSA was further increased to 576.5 $cm^2.cm^{-2}$. These results clearly demonstrated that dealloying has formed a porous nanostructure on the surface, leading to a significant increase in the ECSA.

A proper electrocatalyst must exhibit long-term stability to be practicable at large-scale production during the HER process. Industrial electrochemical water splitting in alkaline media typically operates at current densities range of −100 to −300 $mA.cm^{-2}$ [57]. Therefore,

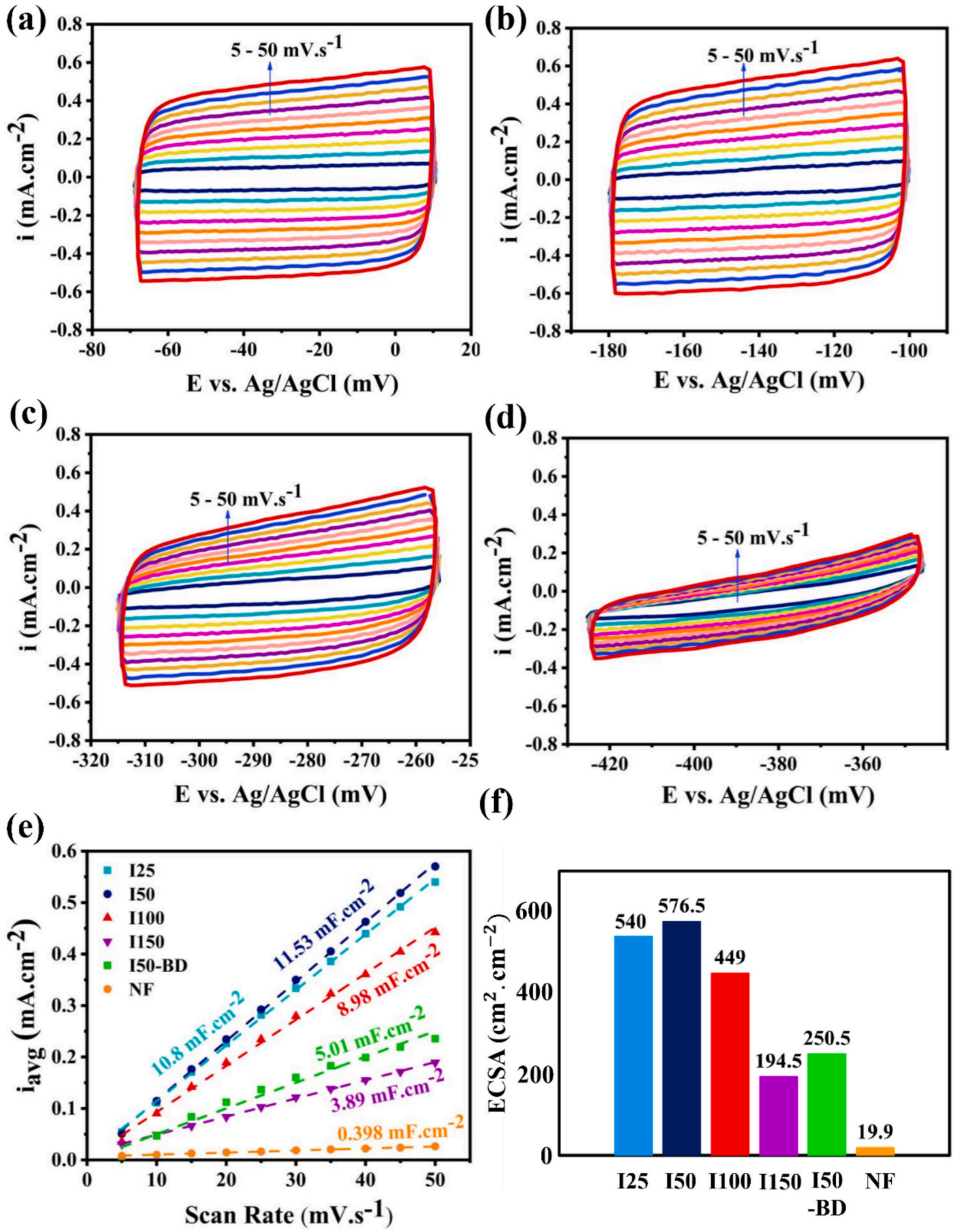

Fig. 7. The CV curves at the scan rates of 5 to 50 mV.s^{-1} for samples (a) I25, (b) I50, (c) I100, (d) I150. (e) The plot of average maximum current density versus the scan rates. (f) The values of ECSA for different samples.

monitoring the required potential at a specific current density is an appropriate method for assessing electrocatalytic stability. Chronopotentiometry examination was carried out to evaluate electrocatalytic stability of the sample I50 in a 1 M KOH solution at a current density of −100 mA.cm^{-2} for 50 h. According to Fig. 8a, the potential on the electrode surface remained steady over time, indicating the suitable stability of dealloyed sample I50. The LSV curves after and before stability examination are shown in Fig. 8b to compare. The results of the sample examined for 50 h indicated that the required overpotential to reach the current densities of −10 and −100 mA.cm^{-2} increased by only 3 and 15 mV, respectively, which are negligible. It confirms a desirable electrocatalytic stability of the sample.

Furthermore, FESEM and mapping analysis were conducted to investigate morphological and compositional stability after the 50 h chronopotentiometry examination. The results, shown in Fig. 8d and e, revealed no damage to the nanostructured coral-like morphology. Moreover, the EDS and elemental mapping results (Fig. 8c and f) demonstrated that the electrode surface retained its homogeneity, with no evidence of chemical changes.

3.3. Oxygen evolution reaction investigation

OER is the anodic reaction of the water splitting. OER is thermodynamically and kinetically more complex than HER, as electron and proton transfers occur in four steps during the process. Therefore, the electrocatalytic activity of the samples for OER was also investigated, to have an electrocatalyst with suitable properties for both HER and OER. The LSV curves for the different dealloyed samples are represented in Fig. 9a. The corresponding Tafel slope curves, and the required overpotentials to reach current densities of 10 and 100 mA.cm^{-2}, along with

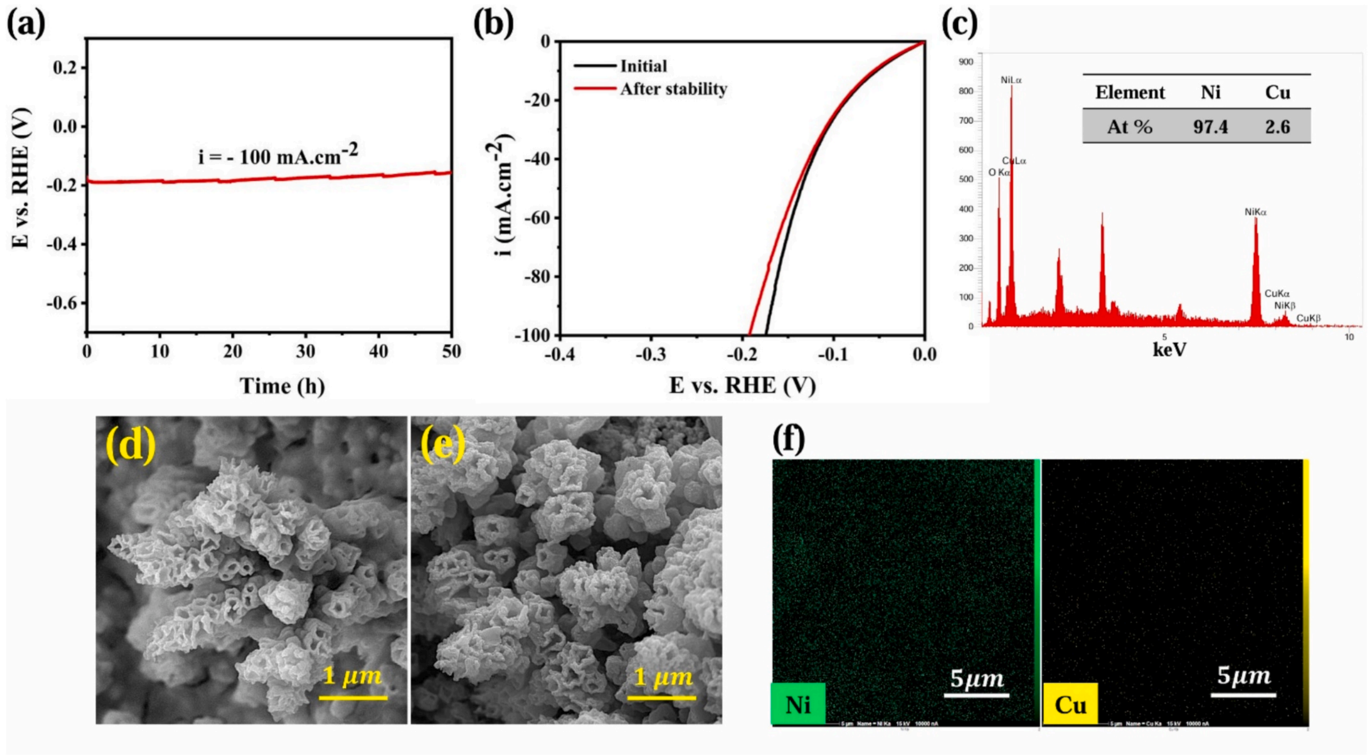

Fig. 8. (a) Chronopotentiometry examination of sample I50 at − 100 mA.cm^{-2} for 50 h; (b) LSV curves of the sample after and before 50 h chronopotentiometry examination; (c) EDS result; (d) and (e) FESEM images of the surface of I50 electrode before and after 50 h chronopotentiometry; and (f) elemental mapping of I50 electrode after chronopotentiometry.

the Tafel slope values, are provided in Fig. 9b and (c), respectively. As observed, the overpotential at a current density of 10 mA.cm^{-2} decreased from 281 to 259 mV as the deposition current density increased from 25 to 100 mA.cm^{-2}. However, as deposition current density increased to 150 mA, the overpotential raised to 274 mV. Sample I100 exhibited the lowest overpotential at a current density of 10 mA.cm^{-2}, with a value of 259 mV. In contrast, the overpotentials for the I25, I50, and I150 samples were 378, 345, and 328 mV, respectively. Same results are obvious for η_{100}. Therefore, the optimal deposition current density for OER was 100 mA.cm^{-2}. The rate of OER were also examined via analyzing Tafel slopes. Sample I100 exhibited the lowest Tafel slope, 55.5 mV.dec^{-1}, which indicates high OER rate on the surface of this electrocatalyst.

To compare the effect of dealloying on electrocatalytic activity for OER, LSV examinations were conducted on the sample I100 before and after dealloying (Fig. 9d) along with results of bare NF. Tafel slopes of these samples are shown in Fig. 9e, and required overpotentials and Tafel slope values are represented in Fig. 9f. The results indicated that depositing a Ni-Cu layer on NF significantly improved the electrocatalytic activity for OER. The required overpotential to reach a current density of 10 mA.cm^{-2} decreased from 479 to 231 mV, while the overpotential to reach 100 mA.cm^{-2} decreased from 688 to 419 mV. After dealloying, the electrocatalytic activity further increased, and the required overpotentials reduced to 259 and 312 mV for current densities of 10 and 100 mA.cm^{-2}, respectively. By comparing the Tafel slopes, the dealloyed sample exhibits the best electrocatalytic activity for OER with a value of 55.5 mV.dec^{-1}.

The EIS examination was conducted to study the rate of the OER on the surface of the electrodes. The obtained Nyquist plots for the various samples at a potential of 1625 mV vs. RHE are shown in Fig. 9g. Additionally, the extracted electrochemical parameters from EIS results are represented in Table S3. As observed, the Nyquist plots for all the samples exhibited a single time constant. Based on the results, the values of R_{ct} for the dealloyed samples I25, I50, I100, and I150 were 0.707, 0.409, 0.337, and 0.369 Ω.cm^2, respectively. Therefore, sample I100 had the lowest R_{ct}, indicating better electrocatalytic activity compared to the other samples, which was also confirmed by the LSV results.

To further investigate the effect of dealloying on the EIS results for OER, the Nyquist plots are plotted for the NF and the sample I100 before and after dealloying at a potential of 1625 mV vs. RHE (Fig. 9h). Electrochemical parameters from the EIS results are represented in Table S3. The values of R_{ct} for the NF, I100 − BD, and I100 were 17.65, 1.384, and 0.337 Ω.cm^2, respectively. The NF exhibited the highest R_{ct}, indicating poor electrocatalytic activity for OER. After depositing the Ni-Cu layer on the NF, the R_{ct} significantly decreased, and after dealloying, the R_{ct} reached its minimum value.

As observed in comparison of the HER and OER results, the optimal sample for HER is not identical to that for OER. The HER in alkaline media occurs on metallic Ni sites capable of H* adsorption, and that increasing the density of these sites directly enhances HER kinetics. Prior work confirms that porous or nanostructured Ni surfaces significantly reduce the free energy of H* adsorption, thus improving HER activity [5]. At current density of 50 mA.cm^{-2}, the moderate deposition rate allows controlled nucleation and growth, leading to a more uniform, porous structure with higher electrochemical surface area (ECSA = 576.5 cm^2.cm^{-2}). The large ECSA provides abundant active sites, which is crucial for HER, since hydrogen evolution benefits directly from the number of accessible catalytic sites for proton adsorption and reduction. However, at current density of 100 mA.cm^{-2}, the faster deposition induces rougher, denser clusters and potentially higher crystallinity/defect incorporation, which lowers the charge transfer resistance (R_{ct} = 0.337 Ω.cm^2). For OER, kinetics are typically limited by sluggish electron transfer in the multi-step oxidation pathway, so a surface with enhanced conductivity and low R_{ct} becomes more beneficial than simply maximizing surface area. In this case, the morphology at 100 mA.cm^{-2} provides better electron transport channels and structural stability during oxygen evolution, favoring OER activity despite the relatively lower ECSA. Additionally, under anodic OER conditions,

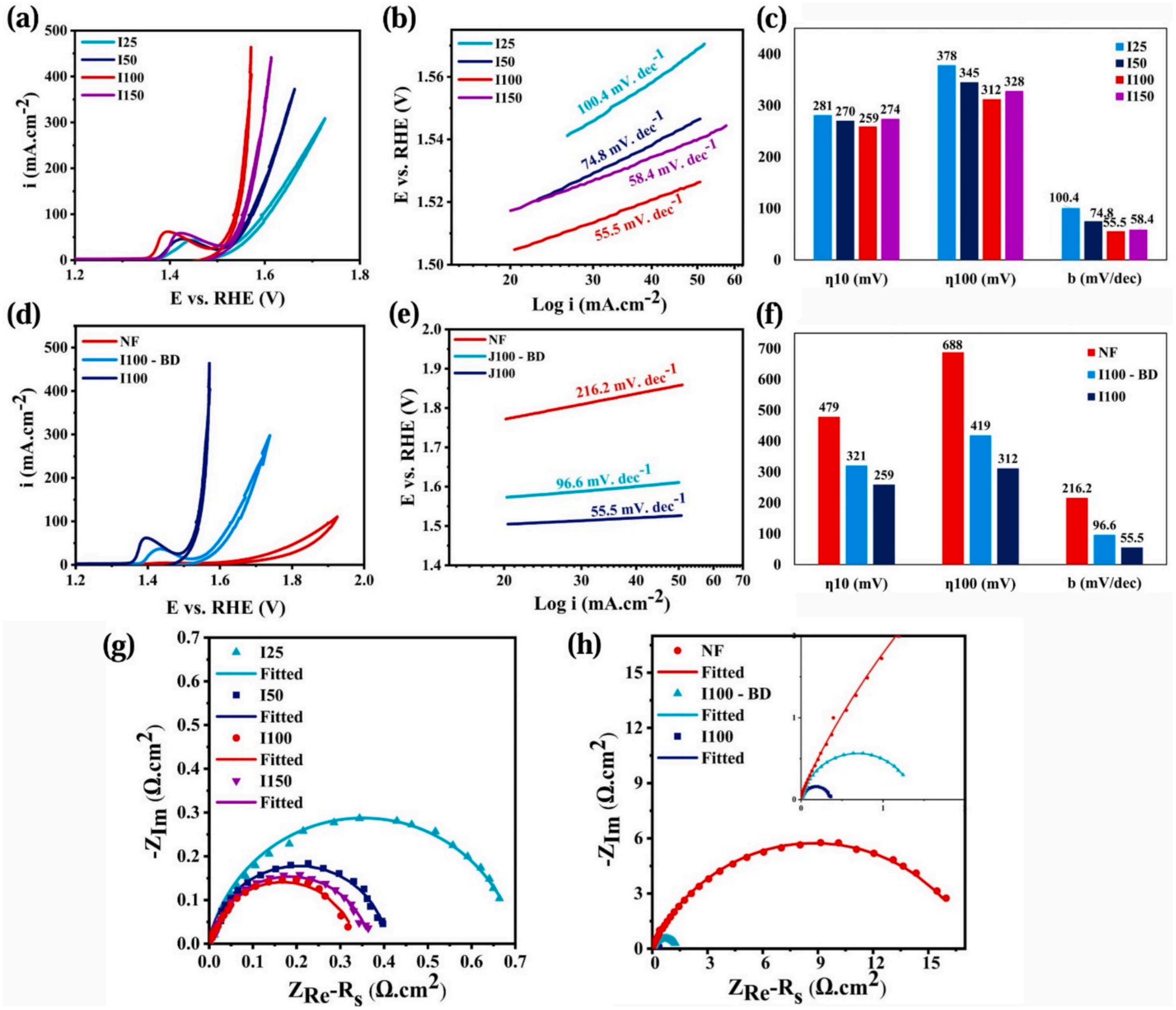

Fig. 9. (a) iR corrected LSV curves for OER, (b) Tafel slopes, and (c) required overpotentials of dealloyed samples. (d) iR corrected LSV curves, (e) Tafel slopes, (f) required overpotentials of NF, I100 − BD, and I100 in 1.0 M KOH solution, (g) Nyquist curves of the dealloyed samples at applied potential of 1625 mV vs. RHE, and (h) Nyquist curves of the different samples at applied potential of 1625 mV vs. RHE.

metallic Ni is known to undergo surface self-reconstruction to form Ni $(OH)_2$/NiOOH, which are the actual OER-active species. Numerous studies show that β-NiOOH is the dominant active phase for OH* adsorption and subsequent O–O bond formation [6]. The I100 sample exhibits the lowest R_{ct}, indicating a surface that facilitates rapid electron transfer through the Ni/NiOOH interface. Additionally, the peaks observed in Fig. 9a indicates the formation of these species during the OER. Thus, even though the porous metallic Ni framework remains after dealloying, the real active sites during OER originate from in-situ generated NiOOH species, supported by the low Tafel slope (55.5 mV. dec^{-1}) typical for NiOOH-mediated OER. Thus, the optimal electrodeposition current density differs because HER is more sensitive to surface area and site density, while OER is more sensitive to charge transfer efficiency.

Fig. 10a represents chronopotentiometry examination of sample I100 at 100 mA.cm^{-2} for 50 h. As shown, sample I100 indicates suitable stability because the potential on the electrode surface remained steady over time. The LSV curves after and before stability are shown in Fig. 10b. The results indicated that the required overpotential to reach the current densities of 10 and 100 mA.cm^{-2} increased by only 4 and 7 mV, respectively. It confirms a desirable electrocatalytic stability of the sample. The results of FESEM before and after stability are shown in Fig. 10d. which revealed no damage to the nanostructured coral-like morphology. Fig. 10c and f demonstrate the EDS and elemental mapping results and show that the electrode surface retained its chemical homogeneity.

Raman spectrum for sample I50 after HER, and sample I100 after OER are shown in Fig. S3. After HER testing the spectrum remains essentially identical to the pristine material, indicating that the cathodic environment does not induce significant oxidation or lattice reconstruction and that HER proceeds on the intact pre-existing surface. By contrast, after OER the Raman spectrum exhibits a strongly intensified and broadened band in the 450–600 cm^{-1} region and a depressed/shifted baseline at higher wavenumbers, which interpret as evidence of oxidative surface reconstruction and the formation of higher-valent NiO and NiOOH species. Such in-situ oxidation is widely observed for transition-metal OER catalysts and has been correlated with the emergence of active OER sites. Depending on the material and conditions, the

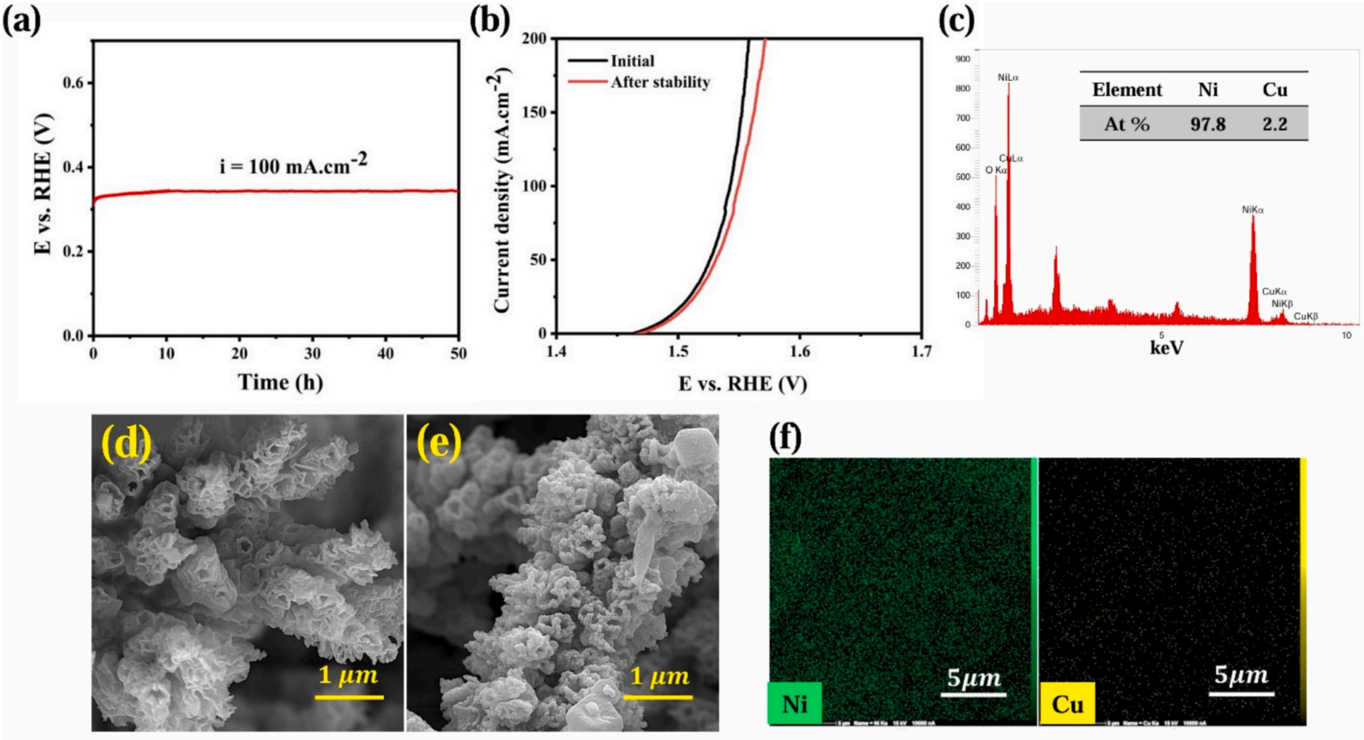

Fig. 10. (a) Chronopotentiometry examination of sample I100 at 100 mA.cm^{-2} for 50 h; (b) LSV curves of the sample after and before 50 h chronopotentiometry examination; (c) EDS result; (d) and (e) FESEM images of the surface of I100 electrode before and after 50 h chronopotentiometry; and (f) elemental mapping of I100 electrode after chronopotentiometry.

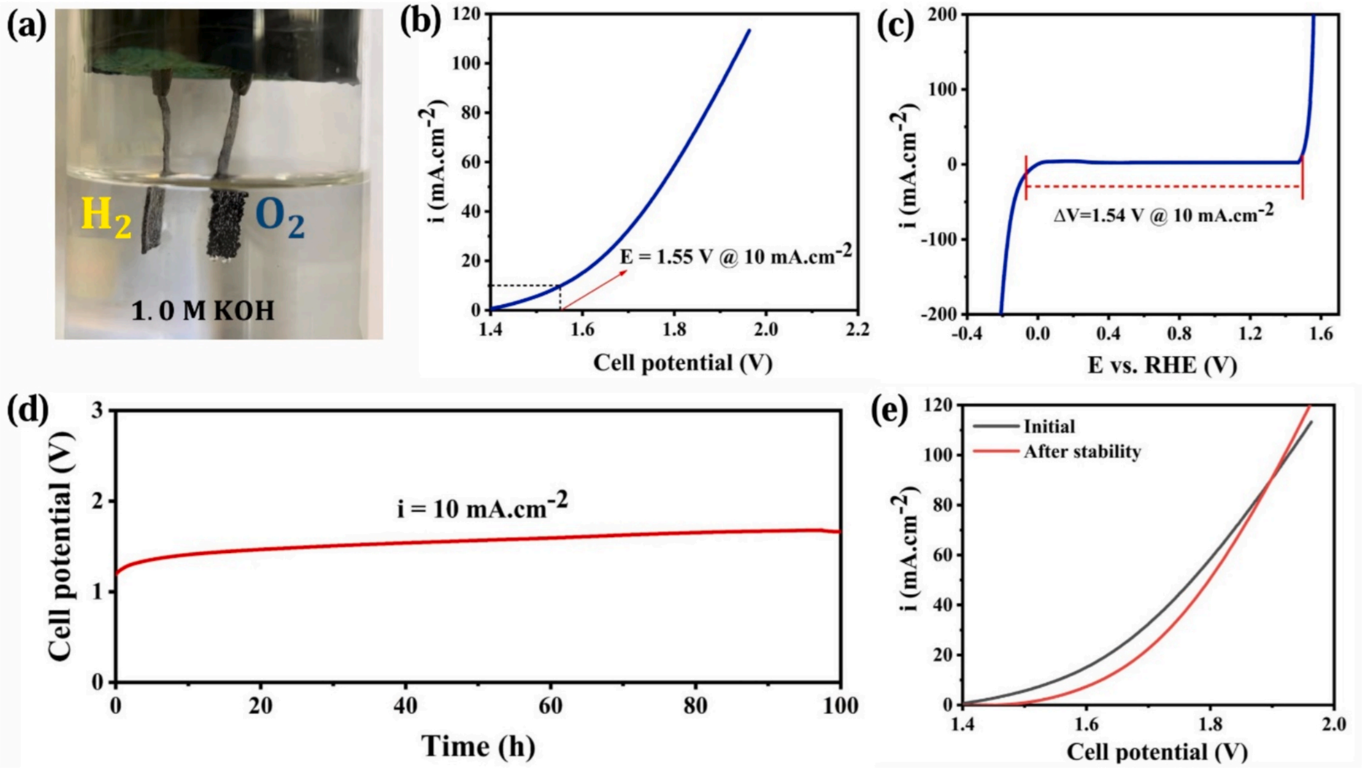

Fig. 11. (a) Schematic of the electrochemical water splitting process, (b) The current density versus cell potential curve for the electrochemical water splitting, (c) Overall water splitting curve obtained from OER and HER, (d) Chronopotentiometry examination for overall water splitting over 100 h; (b) The current density versus cell potential curve for before and after chronopotentiometry examination.

oxidized surface may favor the conventional adsorbate evolution mechanism (AEM) by modifying adsorbate binding energies, or enable lattice-oxygen participation (LOM) where lattice oxygen directly contributes to O–O bond formation [59].

3.4. Water splitting

Based on the favorable performance of electrodeposited electrocatalysts through the dealloying method for HER and OER, these electrodes were utilized as bifunctional electrocatalysts to evaluate their performance in a two-electrode system for electrochemical water splitting. Since samples I50 and I100 were the optimized samples for HER and OER, respectively, these two electrodes were employed as the anode and cathode in the two-electrode system to study overall water splitting reaction. A schematic of the overall water splitting reaction is illustrated in Fig. 11a. The current density versus potential curve in the two-electrode system is represented in Fig. 11b. Based on the results, it was observed that dealloyed electrocatalysts demonstrated favorable activity for the electrochemical water splitting reaction, requiring only 1.55 V to reach a current density of 10 $mA.cm^{-2}$. The required potential for electrochemical water splitting at a current density of 10 $mA.cm^{-2}$ was approximately equal to summation of required applied potential of OER and HER at this current density (1.54 V), as shown in Fig. 11c. This value is lower than those reported in other studies utilizing the dealloying method (Table S4). According to results, it can be concluded that the intrinsic electrocatalytic properties of Ni along with the specific morphology (coral-like) of the dealloyed samples that provided a high ECSA have led to desirable electrocatalytic activity for the overall electrochemical water splitting reaction. The chronopotentiometry examination was conducted for overall water splitting at 10 $mA.cm^{-2}$ for 100 h (Fig. 11d). According to the results, no significant decrease in the overpotential was observed, which indicates the good stability of the electrodes in the alkaline solution. Fig. 11e represents the current density versus cell potential curve for before and after chronopotentiometry examination. The difference of overpotential at current density of 100 $mA.cm^{-2}$ was only 7 mV, which shows a desirable electrocatalytic stability.

4. Conclusion

In this research, a nanostructured Ni-Cu electrocatalyst was synthesized through an electrochemical dealloying method on a conductive NF substrate to use in the electrochemical water splitting process, and its electrocatalytic activity was investigated. The effect of different electrodeposition current densities on the electrocatalytic activity was also studied. FESEM results of dealloyed Ni-Cu electrodes revealed a coral-like morphology, which was due to the selective dissolution of Cu. According to the results, although Cu had a more positive standard electrochemical potential and was more noble, it exhibited higher dissolution rate compared to Ni due to passivity of Ni. The LSV results revealed that the best electrocatalytic activity for HER was obtained for sample deposited at a current density of 50 $mA.cm^{-2}$. The measured HER overpotentials were −57 and −169 mV to reach current densities of −10 and −100 $mA.cm^{-2}$, respectively. Tafel slope of the sample was 65 $mV.dec^{-1}$, indicating its superiority over the other samples. Additionally, the EIS results confirmed the superior electrocatalytic activity of this sample, with an R_{ct} of 1.164 $\Omega.cm^2$ at a potential of −170 mV vs. RHE. Analysis of the ECSA showed that the sample had the highest active surface area which was measured 576.5 $cm^2.cm^{-2}$. Moreover, after long-term stability examination, the dealloyed electrode showed high electrochemical and morphological stability. The results also showed that the best electrocatalyst for the OER was the sample deposited at a current density of 100 $mA.cm^{-2}$. The required OER overpotentials were 259 and 312 mV to achieve current densities of 10 and 100 $mA.cm^{-2}$, respectively. Tafel slope of this sample for the OER was 55.5 $mV.dec^{-1}$, and its R_{ct} was 0.337 $\Omega.cm^2$ at the potential of 1625 mV vs. RHE. Finally, a two-electrode system was used with the best samples to investigate the behavior of the electrocatalysts in the overall water splitting process. The results showed that an applied potential of 1.55 V was required to reach a current density of 10 $mA.cm^{-2}$. Thus, the total overpotential for the water splitting process was 320 mV.

CRediT authorship contribution statement

Narjes Ramezanian: Writing – original draft, Methodology, Investigation. **Mostafa Mirjalili:** Writing – review & editing, Writing – original draft, Validation, Supervision, Project administration, Methodology, Investigation, Funding acquisition, Formal analysis. **Ghasem Barati Darband:** Writing – review & editing, Writing – original draft, Supervision, Project administration, Methodology, Investigation, Funding acquisition, Formal analysis.

Declaration of competing interest

The authors declare that they have no known competing financial interests or personal relationships that could have appeared to influence the work reported in this paper.

Appendix A. Supplementary material

Supplementary data to this article can be found online at https://doi.org/10.1016/j.fuel.2026.138309.

Data availability

Data will be made available on request.

References

[1] Khan MA, Zhao H, Zou W, Chen Z, Cao W, Fang J, et al. Recent progresses in electrocatalysts for water electrolysis. Electrochem Energy Rev 2018;1:483–530.

[2] Li A, Sun Y, Yao T, Han H. Earth-abundant transition-metal-based electrocatalysts for water electrolysis to produce renewable hydrogen. Chemistry–A. Eur J 2018;24(69):18334–55.

[3] Lewis NS, Nocera DG. Powering the planet: chemical challenges in solar energy utilization. Proc Natl Acad Sci 2006;103(43):15729–35.

[4] Hunter BM, Gray HB, Muller AM. Earth-abundant heterogeneous water oxidation catalysts. Chem Rev 2016;116(22):14120–36.

[5] Seh ZW, Kibsgaard J, Dickens CF, Chorkendorff I, Nørskov JK, Jaramillo TF. Combining theory and experiment in electrocatalysis: Insights into materials design. Science 2017;355(6321):eaad4998.

[6] Song J, Wei C, Huang Z-F, Liu C, Zeng L, Wang X, et al. A review on fundamentals for designing oxygen evolution electrocatalysts. Chem Soc Rev 2020;49(7):2196–214.

[7] Ishaq H, Dincer I. Comparative assessment of renewable energy-based hydrogen production methods. Renew Sustain Energy Rev 2021;135:110192.

[8] Winter C-J. Hydrogen energy—abundant, efficient, clean: a debate over the energy-system-of-change. Int J Hydrogen Energy 2009;34(14):S1–52.

[9] Dresselhaus MS, Thomas I. Alternative energy technologies. Nature 2001;414(6861):332–7.

[10] Buchanan M, Crabtree G, Dresselhaus M. The hydrogen economy. Phys Today 2004;57:39–44.

[11] Darband GB, Aliofkhazraei M, Rouhaghdam AS. Nickel nanocones as efficient and stable catalyst for electrochemical hydrogen evolution reaction. Int J Hydrogen Energy 2017;42(21):14560–5.

[12] Esmailzadeh S, Shahrabi T, Darband GB, Yaghoubinezhad Y. Pulse electrodeposition of nickel selenide nanostructure as a binder-free and high-efficient catalyst for both electrocatalytic hydrogen and oxygen evolution reactions in alkaline solution. Electrochim Acta 2020;334:135549.

[13] Gupta S, Patel MK, Miotello A, Patel N. Metal boride-based catalysts for electrochemical water-splitting: a review. Adv Funct Mater 2020;30(1):1906481.

[14] Zou X, Zhang Y. Noble metal-free hydrogen evolution catalysts for water splitting. Chem Soc Rev 2015;44(15):5148–80.

[15] Chen Z, Duan X, Wei W, Wang S, Ni B-J. Iridium-based nanomaterials for electrochemical water splitting. Nano Energy 2020;78:105270.

[16] Zou X, Su J, Silva R, Goswami A, Sathe BR, Asefa T. Efficient oxygen evolution reaction catalyzed by low-density Ni-doped $Co_3 O_4$ nanomaterials derived from metal-embedded graphitic $C_3 N_4$. Chem Commun 2013;49(68):7522–4.

[17] Cheng F, Shen J, Peng B, Pan Y, Tao Z, Chen J. Rapid room-temperature synthesis of nanocrystalline spinels as oxygen reduction and evolution electrocatalysts. Nat Chem 2011;3(1):79–84.

[18] Rezaei B, Jahromi ART, Ensafi AA. Porous magnetic iron-manganese oxide nanocubes derived from metal organic framework deposited on reduced graphene oxide nanoflake as a bi-functional electrocatalyst for hydrogen evolution and oxygen reduction reaction. Electrochim Acta 2018;283:1359–65.

[19] Ji Y, Yang L, Ren X, Cui G, Xiong X, Sun X. Nanoporous CoP$_3$ nanowire array: acid etching preparation and application as a highly active electrocatalyst for the hydrogen evolution reaction in alkaline solution. ACS Sustain Chem Eng 2018;6(9):11186–9.

[20] Carmo M, Fritz DL, Mergel J, Stolten D. A comprehensive review on PEM water electrolysis. Int J Hydrogen Energy 2013;38(12):4901–34.

[21] Jiao Y, Zheng Y, Jaroniec M, Qiao SZ. Design of electrocatalysts for oxygen-and hydrogen-involving energy conversion reactions. Chem Soc Rev 2015;44(8):2060–86.

[22] You B, Sun Y. Chalcogenide and phosphide solid-state electrocatalysts for hydrogen generation. ChemPlusChem 2016;81(10):1045–55.

[23] Zhu YP, Guo C, Zheng Y, Qiao S-Z. Surface and interface engineering of noble-metal-free electrocatalysts for efficient energy conversion processes. Acc Chem Res 2017;50(4):915–23.

[24] Liu L, Zeng G, Chen J, Bi L, Dai L, Wen Z. N-doped porous carbon nanosheets as pH-universal ORR electrocatalyst in various fuel cell devices. Nano Energy 2018;49:393–402.

[25] Shi L, Ling C, Ouyang Y, Wang J. High intrinsic catalytic activity of two-dimensional boron monolayers for the hydrogen evolution reaction. Nanoscale 2017;9(2):533–7.

[26] Zhang H, Yu L, Chen T, Zhou W, Lou XW. Surface modulation of hierarchical MoS$_2$ nanosheets by Ni single atoms for enhanced electrocatalytic hydrogen evolution. Adv Funct Mater 2018;28(51):1807086.

[27] Zhou P, Zhang Y, Ye B, Qin S, Zhang R, Chen T, et al. MoP/Co2P hybrid nanostructure anchored on carbon fiber paper as an effective electrocatalyst for hydrogen evolution. ChemCatChem 2019;11(24):6086–91.

[28] Maleki M, Sabour Rouhaghdam A, Barati Darband G, Han D, Shanmugam S. Highly active and durable NiCoSeP nanostructured electrocatalyst for large-current-density hydrogen production. ACS Appl Energy Mater 2022;5(3):2937–48.

[29] Angeles-Olvera Z, Crespo-Yapur A, Rodríguez O, Cholula-Díaz JL, Martínez LM, Videa M. Nickel-based electrocatalysts for water electrolysis. Energies 2022;15(5):1609.

[30] Yang F, Tian X, Luo W, Feng L. Alkaline hydrogen oxidation reaction on Ni-based electrocatalysts: from mechanistic study to material development. Coord Chem Rev 2023;478:214980.

[31] Huo L, Jin C, Jiang K, Bao Q, Hu Z, Chu J. Applications of nickel-based electrocatalysts for hydrogen evolution reaction. Adv Energy Sustainability Res 2022;3(4):2100189.

[32] Modghan NS, Mirjalili M, Moayed MH, Barati DG. Tailoring the active sites of nanosheet NiSe/NiSe$_2$ catalyst by pulse electrodeposition on the 3D microporous Ni-Cu/NF substrate for both hydrogen and oxygen evolution reactions. J Electrochem Soc 2024.

[33] Modghan N-S, Mirjalili M, Moayed M-H, Darband GB. A suitable porous micro/nanostructured Cu and Cu–Ni film: evaluation of electrodeposition behavior, electrocatalytic activity, and surface characterization of porous film. J Electrochem Soc 2023;170(7):076506.

[34] Qiao Y, Peng M, Lan J, Jiang K, Chen D, Tan Y. Active-site engineering in dealloyed nanoporous catalysts for electrocatalytic water splitting. J Mater Chem A 2023;11(2):495–511.

[35] Anantharaj S, Noda S. Electrochemical dealloying-assisted activity enhancement: the next big thing in water electrosplitting! Nano Energy 2023;114:108624.

[36] Chen Y, Tan Z, Wang E, Yin J, Luo L, Shen S, et al. Progress and prospects of dealloying methods for energy-conversion electrocatalysis. Dalton Trans 2023;52(22):7370–82.

[37] Sang Q, Hao S, Han J, Ding Y. Dealloyed nanoporous materials for electrochemical energy conversion and storage. EnergyChem 2022;4(1):100069.

[38] Kumar A, Purkayastha SK, Guha AK, Das MR, Deka S. Designing nanoarchitecture of NiCu dealloyed nanoparticles on hierarchical Co nanosheets for alkaline overall water splitting at low cell voltage. ACS Catal 2023;13(16):10615–26.

[39] Weissmüller J, Sieradzki K. Dealloyed nanoporous materials with interface-controlled behavior. MRS Bull 2018;43:14.

[40] Teng X, Wang J, Ji L, Lv Y, Chen Z. Ni nanotube array-based electrodes by electrochemical alloying and de-alloying for efficient water splitting. Nanoscale 2018;10(19):9276–85.

[41] Niu J, Yue Y, Yang C, Wang Y, Qin J, Zhang X, et al. Ultrarapid synthesis Ni-Cu bifunctional electrocatalyst by self-etching electrodeposition for high-performance water splitting reaction. Appl Surf Sci 2021;561:150030.

[42] Xiong Y, He P. A review on electrocatalysis for alkaline oxygen evolution reaction (OER) by Fe-based catalysts. J Mater Sci 2023;58(5):2041–67.

[43] Ifkovits ZP, Evans JM, Meier MC, Papadantonakis KM, Lewis NS. Decoupled electrochemical water-splitting systems: a review and perspective. Energ Environ Sci 2021;14(9):4740–59.

[44] Sun H, Xu X, Kim H, Jung W, Zhou W, Shao Z. Electrochemical water splitting: Bridging the gaps between fundamental research and industrial applications. Energ Environ Mater 2023;6(5):e12441.

[45] Sun Q, Dong Y, Wang Z, Yin S, Zhao C. Synergistic nanotubular copper-doped nickel catalysts for hydrogen evolution reactions. Small 2018;14(14):1704137.

[46] Li Y, Dastafkan K, Sun Q, Ma Y, Wang X, Yang X, et al. Ni-based 3D hierarchical heterostructures achieved by selective electrodeposition as a bifunctional electrocatalyst for overall water splitting. Electrochim Acta 2021;379:138042.

[47] Hassanizadeh E, Mirjalili M, Moayed MH, Darband GB. Ultra-fast electrodeposition of dynamic hydrogen bubble template nickel sulfide on a porous copper layer as an electrocatalyst toward hydrogen evolution reaction. Int J Hydrogen Energy 2024;55:729–39.

[48] Lin R, Zhang J, Lu Q. Influence of electrodeposition-dealloying and silver nanoparticles on the electrochemical properties of nanoporous NiO films for supercapacitor. Chem Eng J 2024;494:153244.

[49] Zhang J, Lin R, Lu Q. Influence of electrodeposition and dealloying on electrochemical properties of porous nickel oxide. Materialia 2025. 102589.

[50] Erlebacher J. An atomistic description of dealloying: porosity evolution, the critical potential, and rate-limiting behavior. J Electrochem Soc 2004;151(10):C614.

[51] McCue I, Benn E, Gaskey B, Erlebacher J. Dealloying and dealloyed materials. Annu Rev Mat Res 2016;46(1):263–86.

[52] Beverskog B, Puigdomenech I. Revised Pourbaix diagrams for copper at 25 to 300 C. J Electrochem Soc 1997;144(10):3476.

[53] Wang K, Lin Z, Tang Y, Tang Z, Tao C-L, Qin D-D, et al. Selenide/sulfide heterostructured NiCo$_2$Se$_4$/NiCoS$_4$ for oxygen evolution reaction, hydrogen evolution reaction, water splitting and Zn-air batteries. Electrochim Acta 2021;368:137584.

[54] Bockris JM. Modern aspects of electrode kinetics. Annu Rev Phys Chem 1954;5(1):477–500.

[55] Samantara AK, Ratha S. Metal oxides/chalcogenides and composites: emerging materials for electrochemical water splitting. Springer; 2019.

[56] He J, Hu B, Zhao Y. Superaerophobic electrode with metal@ metal-oxide powder catalyst for oxygen evolution reaction. Adv Funct Mater 2016;26(33):5998–6004.

[57] Nazemi SM, Darband G, Davoodi A. Interfacial engineering of Ni-Co-Mn@Ni nanosheets-nanocones arrays for high performance non-noble metal electrocatalyst for hydrogen generation. Nanoscale 2024;16.

[58] Anantharaj S, Sugime H, Noda S. Why shouldn't double-layer capacitance (Cdl) be always trusted to justify Faradaic electrocatalytic activity differences? J Electroanal Chem 2021;903:115842.

[59] Ren X, Zhai Y, Yang N, Wang B, Liu S. Lattice oxygen redox mechanisms in the alkaline oxygen evolution reaction. Adv Funct Mater 2024;34(32):2401610.